JOURNAL OF GEOPHYSICAL RESEARCH, VOL. 112, D24206, doi:10.1029/2007JD008711, 2007

Comparing irradiance fields derived from Moderate Resolution Imaging Spectroradiometer airborne simulator cirrus cloud retrievals with solar spectral flux radiometer measurements

K. Sebastian Schmidt,[1] Peter Pilewskie,[1] Steven Platnick,[2] Gala Wind,[2,3] Ping Yang,[4] and Manfred Wendisch[5]

Received 27 March 2007; revised 12 August 2007; accepted 12 September 2007; published 28 December 2007.

[1] During the Cirrus Regional Study of Tropical Anvils and Cirrus Layers–Florida Area Cirrus Experiment, the Moderate Resolution Imaging Spectroradiometer (MODIS) airborne simulator (MAS) and the solar spectral flux radiometer (SSFR) operated on the same aircraft, the NASA ER-2. While MAS provided two-dimensional horizontal fields of cloud optical thickness and effective ice particle radius, the SSFR measured spectral irradiance in the visible to near-infrared wavelength range (0.3–1.7 μm). The MAS retrievals, along with vertical profiles from a combined radar/lidar system on board the same aircraft were used to construct three-dimensional cloud fields, which were input into Monte Carlo radiative transfer models. The simulated field of spectral albedo (ratio of reflected upwelling to incident downwelling irradiance) was compared with the SSFR measurements. For two cases, the relative importance of spatial cloud heterogeneities, various approximations of the single scattering parameters, vertical structure, cirrus optical thickness, and ice crystal effective radius was studied.

Citation: Schmidt, K. S., P. Pilewskie, S. Platnick, G. Wind, P. Yang, and M. Wendisch (2007), Comparing irradiance fields derived from Moderate Resolution Imaging Spectroradiometer airborne simulator cirrus cloud retrievals with solar spectral flux radiometer measurements, *J. Geophys. Res.*, *112*, D24206, doi:10.1029/2007JD008711.

1. Introduction

[2] Clouds exert a strong radiative forcing on Earth's climate. Their net cooling effect is three to five times as large as the expected warming from a CO_2 doubling [*Ramanathan et al.*, 1989]. However, their impact on future climate is difficult to predict. Although climate models are now showing a positive (destabilizing) cloud feedback to warming, there remains a large uncertainty in the prediction of cloud amount and hence in its magnitude [*Soden and Held*, 2006]. The cloud radiative forcing measured in radiative budget experiments varies from -27 W m^{-2} [*Ardanuy et al.*, 1991] to -19 W m^{-2} [*Kiehl et al.*, 1994], depending on time span and coverage.

[3] Satellite sensors mostly measure radiance, that is, the radiative energy density related to a fractional solid angular range, covering only a small part of the respective hemisphere. However, for energy budget considerations a radiation quantity is needed that contains the cosine-weighted radiance integrated over the entire upper and lower hemisphere (irradiance). For estimating the radiative budget globally on the basis of satellite observations, a conversion from satellite radiance measurements to irradiance is required. For example, the Clouds and the Earth's Radiant Energy System (CERES) project [*Wielicki et al.*, 1998] derives top-of-atmosphere broadband irradiance from broadband radiance observations. The CERES algorithms use statistical angular distribution models [*Loeb et al.*, 2005] coupled with spectral radiance observations from the Moderate Resolution Imaging Spectroradiometer (MODIS) [*King et al.*, 1992] to identify and characterize a 20 km CERES scene. Considering the importance of clouds in the climate system, a validation of radiance-derived irradiance with measurements is of primary significance.

[4] In the study reported here, we use airborne measurements of spectral irradiance from the solar spectral flux radiometer (SSFR) [*Pilewskie et al.*, 2003] to compare with calculated irradiance derived from cirrus cloud retrievals using the MODIS airborne simulator (MAS) [*King et al.*, 2004]. We thus quantify the ability to convert spectral radiance measurements to irradiance through radiative transfer calculations, given the associated limitations of the measurements. In contrast to the statistical approach in CERES or Earth Radiation Budget Experiment (ERBE) [*Barkstrom*, 1984], our method is tested for two specific cloud scenes as observed by the aircraft. Our goal is to determine the suitability of radiance-derived cirrus and anvil

[1] Laboratory for Atmospheric and Space Physics, University of Colorado, Boulder, Colorado, USA.
[2] NASA Goddard Space Flight Center, Greenbelt, Maryland, USA.
[3] SSAI, Inc., Lanham, Maryland, USA.
[4] Department of Atmospheric Sciences, Texas A&M University, College Station, Texas, USA.
[5] Institute for Atmospheric Physics, Johannes Gutenberg University of Mainz, Mainz, Germany.

0148-0227/07/2007JD008711$09.00

cirrus retrievals for quantifying the radiative energy budget. We test radiance-to-irradiance conversions on a fundamental level by including microphysical structure and cloud inhomogeneities, and by using the spectral irradiance measurements to help understand the physical basis for any discrepancies with imager-derived irradiances.

[5] We use data from the Cirrus Regional Study of Tropical Anvils and Cirrus Layers–Florida Area Cirrus Experiment (CRYSTAL-FACE) in July 2002, where the SSFR and MAS flew on the NASA high-altitude ER-2, along with a combined radar/lidar system for cloud profiling [*McGill et al.*, 2004]. Previously, *Wendisch et al.* [2005] carried out one-dimensional (1-D) model calculations using ice crystal measurements on the NASA WB-57 (in close coordination with ER-2) as input, and compared those to closely collocated SSFR spectral irradiance measurements, to study the impact of ice crystal shape on solar spectral irradiance. We attempt to determine the relative sensitivity of the irradiance along the ER-2 flight track to the retrieved cirrus cloud optical thickness and its horizontal variability, crystal size and shape, vertical cloud structure, spatial resolution, and boundary conditions. We use ER-2 flight legs from 9 July 2002 (above a fairly homogeneous overcast cirrus cloud with high cloud optical thickness over ocean) and 23 July 2002 (inhomogeneous cirrus case with broken clouds of low to moderate optical thickness over both land and ocean).

[6] In section 2, we describe the SSFR and MAS, the method generating the required cloud fields, and the radiative transfer code applied in this paper. In section 3, sensitivity results are presented. Subsequently, we show the results for the overcast and broken cloud case. In section 5, conclusions are drawn.

2. Methods, Instruments, and Model

[7] To reproduce the irradiance fields measured by the SSFR along the flight track (section 2.1.), 2-D horizontal MAS retrievals of cloud optical thickness and crystal/droplet effective radius (section 2.2.) are used as primary input for generating cloud fields (section 2.3.). As auxiliary parameter, the vertical profile is obtained from a composite of the cloud physics lidar (CPL), and a cloud radar [*McGill et al.*, 2004]. The cloud fields are used as input to 3-D radiative transfer calculations (section 2.4.). The model results along the flight track are compared with SSFR measurements along this same line.

2.1. SSFR

[8] The SSFR [*Pilewskie et al.*, 2003] is composed of a pair of identical spectrometers responsive in the spectral region between 300 nm and 1700 nm. The identical pairs of Zeiss monolithic miniature spectrometer modules (visible wavelength range (MMS-1) and near-infrared wavelength range (MMS-NIR)) were used for simultaneous zenith and nadir viewing. The MMS-1 modules were temperature stabilized at 27°C ± 0.3°C and the MMS-NIR were thermoelectrically cooled to 0°C. Spectral resolution was about 8 nm for the MMS-1 and about 12 nm for the MMS-NIR. In-flight integration time for the each of the spectrometers was nominally 100 ms and the spectral sampling rate was approximately 1 Hz. The SSFR was calibrated for wavelength and angular response, as well as absolute spectral irradiance. Estimated root mean square uncertainty was 3% to 5% for the SSFR spectral range between 350 and 1700 nm; precision was between 0.1% and 0.3%.

[9] The spectral irradiance reflected at cloud top was normalized by the downwelling spectral irradiance to determine the spectral albedo of the cloud. For hemispheric irradiance measurements, assuming an isotropic radiation field, 71% of the measured signal originates from within 45 degrees of normal incidence. Therefore we define the SSFR footprint containing 71% of the nadir signal to be a circle of radius equal to the distance from the aircraft to cloud. For the cases under discussion the footprint radii are approximately 6–7 km which is covered by the MAS swath. The other 29% originate, in part, from beyond the MAS track.

2.2. MAS

[10] The MAS is a scanning spectrometer with fifty spectral channels divided into four ports that cover a range between 470 nm and 14.2 μm. At nominal ER-2 altitudes, MAS has a spatial ground resolution of 50 m (nadir) and a swath of 37 km (±43 degrees scan). The solar band radiometry calibration is done with an integrating sphere; an integrating hemisphere is used to monitor trends in the field. The MAS retrieval approach [*Platnick et al.*, 2001] (originally developed for water clouds) is based on information about cloud optical thickness mainly in the 0.65 μm and 0.86 μm bands and effective particle radius information in the 2.1 μm channel, using lookup tables. These libraries contain reflectance values for ice and water clouds corresponding to various bands, and sets of viewing/solar geometries for each optical thickness and effective radius. The surface albedo is also included in the libraries. It is assumed to be a constant value of 0.05 over ocean surfaces for all channels (assuming diffuse illumination of the ocean surface under the cloud) and a constant value per band for land surfaces, which varies between 0.05 for the 0.65 μm channel to 0.25 for the 1.6 μm and the 2.1 μm channels.

[11] Including the ice phase in the retrieval required a set of ice cloud models for generating the forward radiative transfer calculations as well as improved phase discrimination. The libraries of ice crystal microphysical and optical properties required for cloud reflectance and transmittance radiative transfer simulations were derived from ice cloud models used in collection 4 processing of the MODIS operational cloud product (product name MOD06 and MYD06 for MODIS Terra and Aqua, respectively [*Platnick et al.*, 2003]). The collection 4 ice models consisted of 12 ice crystal size distributions composed of four habits (aggregates, bullet rosettes, hollow columns, and plates) with the fraction of each habit in individual size distribution bins being a function of particle effective radius that is defined as follows:

$$r_{eff} = \frac{3}{4}\frac{\langle V \rangle}{\langle A \rangle} \tag{1}$$

where $\langle V \rangle$ and $\langle A \rangle$ are the mean particle volume and projected area for the ice crystal size distribution. Scattering calculations were made using the techniques of *Yang and Liou* [1996].

[12] There are two important differences between the MAS and MODIS collection 4 ice models. First, new scattering calculations for the 12 MODIS cloud models were made using MAS-specific spectral band passes. Second, a quadratic polynomial was fitted to all scattering parameters (single scattering, albedo, asymmetry parameter, and extinction efficiency) as a function of ice crystal effective radius for the 12 models. This served two purposes. The fit smoothed out the slight nonmonotonic behavior with particle effective radius that was problematic in the 3.7 μm band for collection 4 models; it also prevented abrupt changes in the slope or curvature of the scattering parameter in other spectral bands, which can result in nonunique solutions. The nonmonotonic behavior is highly dependent on the limited way the ice crystal habit combinations were selected in collection 4 ice models. New collection 5 models, not available in time for this study, do not have these nonmonotonic features. For collection 4, measures were taken to respace the libraries to ease some of the nonmonotonic curvature created by the original library space: The forward models, based on actual in situ size distributions, had very close spacing of effective radii in portions of the effective radius space, exacerbating the effect of changing slopes/curvatures on retrievals. Therefore, using the quadratic fit, libraries were calculated at equal intervals in interpolated r_{eff} space (5, 10. . . 55, 60 μm). With this approach, we have essentially averaged over the limited collection 4 in situ cloud models in such a way as to create libraries that can provide unique size retrievals and for which the retrieval uncertainty is not affected by sudden changes in scattering properties with effective radius. This approach served as the basis for the MODIS collection 5 ice libraries (for further details, see *Baum et al.* [2005]).

[13] The thermodynamic phase algorithm for MAS data includes tests that infer the location of the MAS band corresponding to the peak reflectance in the 1.6 and 2.1 μm spectral windows (based on the technique of *Pilewskie and Twomey* [1987]). MAS reflectance ratios of 1.66/1.61 μm and 2.25/2.15 μm bands were used as a proxy for the general location of the reflectance peak. The location of these peaks, as shown by *Pilewskie and Twomey* [1987], are sensitive to water thermodynamic phase because of the difference between the bulk absorption spectra of liquid water and ice. These in-band phase retrievals, which are independent of absolute calibration, were compared to a MODIS-like algorithm that uses a combination of IR and/or shortwave-IR (SWIR) tests [*King et al.*, 2004]. Two ER-2 flight tracks are discussed in section 4. There was no difference between the various phase retrievals for the overcast case study (9 July 2002). For the inhomogeneous cloud case study (23 July 2002), the latter half of the track includes multilayer scenes with broken water clouds underneath extensive cirrus. For this situation, there is disagreement among the phase retrievals that is, in part, a consequence of attempting to assign a unique phase to a multilayer/multiphase scene.

[14] The MAS cloud mask is based on the MODIS mask, using a series of threshold tests to detect the presence of clouds with 4 confidence levels [*Ackerman et al.*, 1998]. The confidence levels are: confident cloudy (>99% certainty of cloudiness), probably cloudy (>66% certainty of cloudiness), probably clear (>66% certainty of clear sky), confident clear (>99% certainty of clear sky). The first two confidence levels are treated as 'cloudy' by the MAS retrieval code and the thermodynamic phase determination and subsequent retrieval of optical and microphysical properties is attempted.

[15] MODIS operational cloud top properties are derived from a CO_2 slicing technique [*Menzel et al.*, 1983] for middle to upper level cloud layers and an infrared window band for low-level clouds [*Platnick et al.*, 2003]. Unfortunately, the capability of the MODIS-like technique was limited to mid to high-level clouds during the CRYSTAL-FACE experiment due to insufficient signal-to-noise in some bands and MAS-specific algorithm issues. Therefore, in order to provide a spatially complete cloud top retrieval for all cloud heights, MAS cloud top properties retrievals were derived from path absorption in the 0.94 μm water vapor band. The uncertainties of this method are dependent on the thickness of the cloud and currently being studied. National Centers for Environmental Prediction Global Data Assimilation System (NCEPGDAS) profiles [*Derber et al.*, 1991] were then used to convert the retrieved above cloud vapor amount to cloud top pressure and temperature. While cloud top height is important in its own right, it is also used for atmospheric corrections in the optical and microphysical retrievals.

[16] For the cloud generator discussed in section 2.3., the MAS cloud top height product was only used for the overcast case; for the scattered cloud case, the supplementary lidar data was used along the ER-2 flight track. Both the water vapor and the CO_2 slicing cloud top approaches are applicable only to single layer clouds with known surface reflectance or upwelling emission, respectively, though they have different sensitivities to underlying lower level clouds with the 0.94 μm being more sensitive. As such, the difference between the two algorithms can be an indication of a multilayer scene. As previously discussed, multilayer phase clouds also tend to cause differences in the IR and SWIR phase tests for similar reasons. Using such information, the MAS analysis includes flags of apparent multilayer clouds pixels that can be used to screen the utility of the retrievals that are based on single-layer and single-phase libraries. Of course when the upper layer cloud is too thick, no multilayer information is available.

2.3. Cloud Fields and Surface Albedo

[17] The generated cloud fields were primarily based on the MAS retrievals of 2-D fields of cloud optical thickness, effective crystal/droplet radius, and thermodynamic phase. The 50 m MAS ground spatial resolution translates to somewhat higher resolution at cloud top (about 12–13 km in both cases). The MAS measurements were binned onto a grid with the length of an entire flight leg (350 km and 270 km for the overcast and scattered case, respectively), with a horizontal resolution of 500 m. For this grid box size, the effect of horizontal photon transport between neighbor-

ing pixels was expected to be much smaller than for the original resolution. To check the relative importance of resolution, versions with smaller (100 m) and larger (2000 m) boxes were generated. This sensitivity check relies on retrievals that are potentially already contaminated with in-pixel inhomogeneity biases due to the independent pixel assumption. Because of the larger pixel size of MODIS, results for MAS related to spatial resolution are not necessarily applicable to the spaceborne MODIS.

[18] The clouds simulated in this study were mostly generated from MAS retrievals only. Consequently, no vertical structure was imposed on those clouds (which are thus 2-D fields). However, for determining the impact of vertical structure, various tests were performed. First, a well-defined vertical profile for the cloud extinction or ice crystal effective radius with the same column integrated values as retrieved from MAS was used. Second, cloud top height and vertical structure of cloud extinction were implemented using (1) the MAS retrieved cloud top height for each pixel for the overcast cloud case and (2) the lidar/radar cloud top height along the flight track, as well as geometrical cloud thickness for the scattered cloud case. The lidar/radar matched cloud profile data was not available for case 1, and the MAS cloud top height was not available for case 2. For the overcast case, a separate cloud top height was available for each pixel along the swath. However, no cloud geometrical thickness was available. Therefore the optical thickness was distributed homogeneously over an assumed geometrical thickness of 1 km. For the scattered cloud case, the lidar-retrieved cloud top height was used across the whole swath, as well as the layers given by the lidar and radar measurements. In both cases, the effective radius was kept constant throughout the individual columns.

[19] The cloud simulated for the overcast case consisted of a single ice cloud layer. For the scattered cloud case, there was a region where the retrieved thermodynamic phase was ambiguous. For this region, model runs with a pure ice cloud were compared with a mixed-cloud. At pixels where a second layer was flagged underneath the main cloud sheet, a liquid water cloud was added at 2 km altitude, contributing between 10% and 50% to the column optical thickness.

[20] The 2-D surface albedo was generated from two components: First, the land-use flag from MAS, available for each pixel, was used. Second, two spectral surface albedo data sets from SSFR were available: one above the sea, one above land [*Wendisch et al.*, 2004]. The SSFR-measured surface albedo for sea was mapped onto all pixels flagged with either sea or fresh water. For the rest, including coastal area, the surface albedo for land was used.

2.4. Radiative Transfer Calculations

[21] The single scattering parameters for each grid point were derived from the ice crystal effective radius in three different ways.

[22] 1. The same ray tracing technique as used for the MAS retrievals in this study [*Yang and Liou*, 1996] was applied. For a set of 140 wavelength bands (from 305 nm to 1695 nm, matching the SSFR wavelength range and resolution) and 12 effective crystal radii (6.7 μm to 59 μm) single scattering parameters were calculated. These libraries were used to attribute single scattering albedo and scattering phase function to the effective radius at each grid point. The volume extinction coefficient β and single scattering albedo, ϖ_o, were rescaled using delta transmitted energy δ

$$\beta' = (1 - \delta\varpi_o)\beta \tag{2}$$

and

$$\varpi_o' = \frac{(1-\delta)\varpi_o}{1 - \delta\varpi_o} \tag{3}$$

This is necessary due to δ transmission through parallel planes of crystals at a scattering angle of 0° [*Takano and Liou*, 1989; B. A. Baum, personal communication, 2006].

[23] 2. From the same libraries the asymmetry parameter g (mean cosine of the scattering phase function) was specified for each grid point, which was then used for defining a Henyey-Greenstein scattering phase function. This approach was applied to study the sensitivity of the modeled irradiance field to the distribution of crystal shapes and its specific scattering phase functions, and to the parameterization by a single parameter, g. For high-order multiple scattering, the influence of the individual crystal scattering phase functions on the resulting irradiance field are expected to be negligible [*Wendisch et al.*, 2005]. In particular, no δ scaling was necessary, because the scattering phase function is parameterized in the asymmetry parameter. For 23 July where a mixed-phase cloud was encountered, this method was modified such that for the liquid part, g and ϖ_o were provided by Mie calculations for spherical water droplets. For the solid part, the aforementioned ice crystal libraries were used.

[24] 3. Last, the ice crystals were represented by solid spheres with the given effective radius, and Mie calculations were performed to obtain the scattering phase functions and single scattering albedo.

[25] Atmospheric state variables (1-D) were provided from a combination of ER-2 dropsonde data [*Hock and Franklin*, 1999] below flight altitude, and standard tropical atmosphere [*Anderson et al.*, 1986] above flight altitude.

[26] Two independent 3-D radiative transfer Monte Carlo (MC) models were used in this study. MYSTIC (Monte Carlo code for the physically correct tracing of photons in cloudy atmospheres [*Mayer*, 1999]) and GRIMALDI [*Scheirer and Macke*, 2001]. MYSTIC is embedded in the freely available libRadtran package [*Mayer and Kylling*, 2005; http://www.libRadtran.org]; GRIMALDI is a stand-alone MC code which was applied for method 1 because at the time of this study, MYSTIC could not resolve the forward peak of the ice scattering phase functions with sufficient accuracy. This has meanwhile been fixed (B. Mayer, personal communication, 2007). GRIMALDI was specifically written for applications where the full ice scattering phase function has to be used. MYSTIC was used in all other cases where the ice scattering phase function was not required. For the 500 m resolution, calculations were performed at wavelengths of 500, 745, 1015, 1215, and 1620 nm. For the 100 m and 2000 m resolution, calculations were only done at 500 nm. Both periodic and reflecting

Table 1. Domain-Averaged Properties of the Overcast Cloud Case

Property	Value
Cloud cover	83%
Optical thickness (nonempty points)	92
Effective radius (nonempty points)	23 μm
Cloud albedo for	500 nm, 1620 nm
Measurement (SSFR, 20–250 km)	0.90, 0.26
Model results (20–250 km)	
With exact phase function	0.91, 0.30
With Henyey-Greenstein phase function	0.90, 0.27
With spherical particles (Mie)	0.86, 0.20
With HG and optical thickness/2	0.83, 0.29
With HG and effective radius/2	0.91, 0.41

boundary conditions were applied. Results from periodic boundary conditions are presented. Differences occurred at the boundaries only, and they had no impact on domain-averaged quantities. Additionally, an extended cloud scene was generated for the broken case, extending 40 km beyond the original MAS swath on all sides where cloud optical thickness was set to zero (photons were evenly distributed over the whole extended domain). Depending on horizontal resolution, a photon number between 10^8 and 5×10^8 was used for each wavelength. As top-of-the-atmosphere input, the *Kurucz* [1992] spectrum with 1 nm resolution was used. However, in this paper, only measured and calculated albedos are shown, thus removing any dependence on the exoatmospheric source function, and on the changing solar zenith angle during the measurement. For the overcast case, the mean solar zenith angle of 17° was used (ranging from 15° to 19° during the flight leg). For the scattered cloud case, 77° was used (range 74° to 79°).

3. Sensitivity Tests

[27] When modeling irradiance in this study, we assessed the modeling error due to various factors. The first part consisted in checking the impact of potential retrieval uncertainties. Since the actual uncertainties for each MAS pixel were not yet available when this study was conducted, error propagation analysis was performed by means of a sensitivity analysis of the model results to optical thickness and effective radius. Model runs were performed using halved and doubled values of optical thickness and effective radius, respectively. Secondly, the impact of vertical structure (not available from MAS), and horizontal resolution was determined.

[28] Table 1 shows the domain averaged model results for 500 nm and 1620 nm using (1) the original retrievals, (2) halved optical thickness, and (3) halved effective radius. For 500 nm, the albedo is substantially decreased by halving the optical thickness whereas it is almost not sensitive to the effective radius. For 1620 nm, the opposite is seen: decreasing of the optical thickness has a negligible effect, while halving the effective radius increases the albedo substantially. This is as expected taking into account the fundamental principles of optical cloud remote sensing [*Twomey and Cocks*, 1982]: Cloud optical remote sensing methods usually use as few as two wavelengths: one in the visible part of the spectrum, where absorption by condensed water is negligible such that cloud optical depth can be derived, and the other in the near-infrared spectral range, where water absorbs and thus particle size information is obtained.

[29] With respect to the vertical distribution of extinction coefficient, no noticeable effect on the reflected irradiance was observed when assuming different vertical profiles as long as the column optical thickness was conserved. This is in accordance with similarity relationships [*van de Hulst*, 1980]. This was even true for the scattered cloud case on 23 July 2002 which, in some regions, was composed of two distinct layers (detected by the lidar/radar system). Since no information about the vertical distribution of the effective radius was available, a constant value was assumed. When imposing a vertical profile such as increasing or decreasing effective radius with height, the radius of crystals or drops closest to cloud top most heavily weighted the result, rather than the mean value. A profile with decreasing effective radius with height resulted in an increased albedo for 1620 nm (but not for 500 nm), because the smaller crystals on top (less absorbing) outweighed the larger, more absorbing crystals further down. Since no information on the vertical profile of effective radius was available, a constant value for each column was assumed for the rest of this study. The effect of vertical profiles on the retrievals is discussed by *Platnick* [2000].

[30] The sensitivity of the results to spatial resolution was tested by comparing mean values of reflected and transmitted irradiance and the power spectra of the horizontal distribution of modeled irradiance. Virtually no difference in the mean values and the shape of the power spectra was found for the different spatial resolutions, and a horizontal resolution of 500 m was determined to be sufficient for this study. It should be noted that the MAS cross-track swath account for only 50% of the SSFR integrated field. For the highly homogeneous case (section 4.1.) this had likely negligible impact. In section 4.2 we show that this cannot be overlooked for the scattered cloud case.

4. Results

4.1. Overcast Cloud Case

[31] The overcast cirrus case (9 July 2002 from 1835 to 1902 UTC) was observed by the ER-2 with a flight leg entirely above the Gulf of Mexico. A thick cirrus cloud (optical thickness about 90, ranging from 25 to 150) was probed during the first 270–280 km. Cloud-free conditions were observed at the end of the flight leg. A false color image of the flight track is shown in Figure 1a. The cloud-free regions (over ocean, from 1857 (18.95) UTC) appear in black color; high ice clouds in green shades (the brighter the higher the optical thickness), and liquid water clouds (at about 1858 (18.96) UTC) in white brown. In Figures 1b and 1c (MAS optical thickness and effective radius), the x axis is defined along the flight track, and the y axis ranges from −6 to +6 km across the MAS swath. Both plots show the 500 m resolution version of the data. The fill color (no cloud) is grey. Figure 1d shows an image of the time-dependent spectral albedo measured by the SSFR along the same track. On the vertical axis, the wavelength varies between 350 nm to 1700 nm. Over a large segment of the flight track, the albedo was close to unity over a large wavelength range. Lower albedo values occur for wavelengths near, for example 1600 nm, where absorption

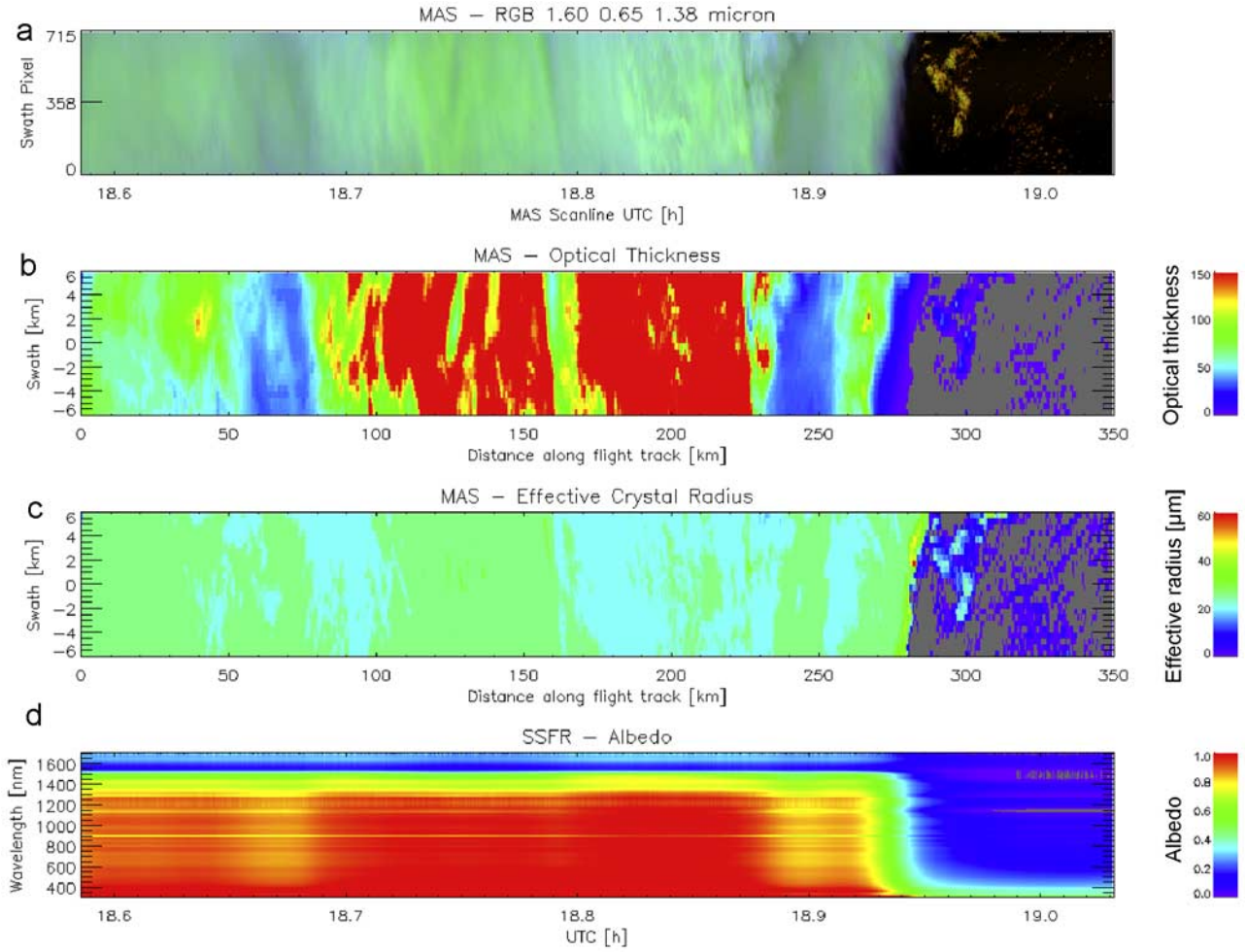

Figure 1. (a) MAS false color image, (b) retrieved cloud optical thickness and (c) effective radius, and (d) SSFR albedo along a leg of 350 km (1835–1902 UTC) on 9 July 2002, mostly above a thick cirrus cloud, partly above water. MAS optical thickness and effective radius are shown for 500 m horizontal cloud resolution.

reduces the reflected irradiance. The grey and blue regions above sea correspond to zero or nearly zero albedo due to complete absorption in the water vapor bands. Note that for thick clouds these bands are filled in (greatly reduced water vapor path) and the absorption maxima are shifted to ice absorption bands, the largest of which occur around 1500 nm.

[32] In contrast to the spatially highly inhomogeneous pattern of the retrieved optical thickness showing considerable structure along and across the flight track, the SSFR albedo is quite smooth at all wavelengths. This is due to geometrical smoothing which occurs between cloud top (13 km) and flight altitude (20 km), and to a lesser extent to reduced sensitivity to small changes in optical thickness for very thick clouds (saturation effect). The cloud albedo is approaching an asymptotic limit, beyond which increasing cloud thickness produces minimal changes.

[33] We also used the independent column approximation for calculating the 3-D irradiance field by switching off horizontal photon transport in the MC model. The measured irradiance scale break was not reproduced in the power spectra for this case (see also *Schmidt et al.* [2007] for water clouds). However, the domain averaged irradiance did not change compared to the case with horizontal photon transport switched on.

[34] Figure 2 shows the measured and simulated albedo for two wavelengths (500 nm, Figure 2, left; 1620 nm, Figure 2, right) along the flight track. The thick red line shows the SSFR measurements. The thin dash-dotted line in the left graph shows the optical thickness, averaged over a footprint with a radius of about 6 km (corresponding to the SSFR footprint radius). Since the corresponding reflected irradiance is almost saturated, even large changes in cloud optical thickness result in small changes in the reflected irradiance only. The lines on the bottom indicate the surface albedo, averaged over the same footprint, and the modeled albedo at 20 km altitude if no clouds were present. The blue line in Figure 2 shows the model results using the exact phase function from *Yang and Liou*'s [1996] ice crystal libraries. The black line represents the results from the Henyey-Greenstein approximation for the phase function. Only small differences are observed between the black and blue curves for both wavelengths. Differences between measurements and simulation at 500 nm wavelength occur

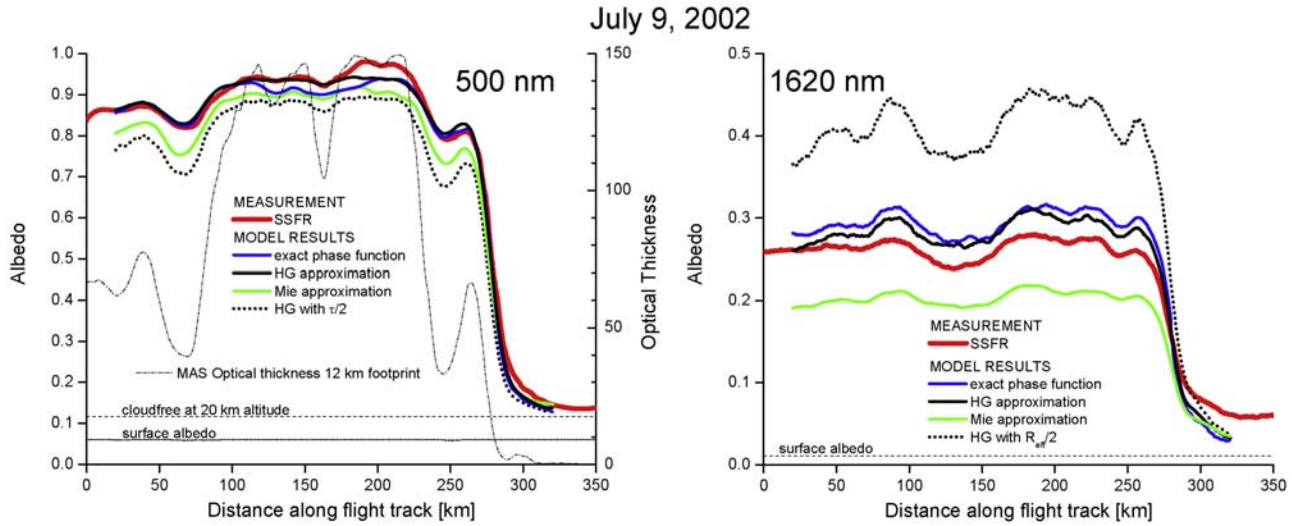

Figure 2. Measured and modeled albedo for 9 July 2002 for 500 nm and 1620 nm.

from 100 to 200 km. One possible explanation is that there are some contributions to SSFR-sampled irradiance from beyond the MAS track (section 2.1). The green line shows the model results based on a Mie representation of the scattering phase function for spherical particles. When halving the effective radius and using the Henyey-Greenstein phase function approximation, there is also almost no change in the modeled albedo (not shown). This is, in part, due to the saturation of the albedo at 500 nm, although albedo at this wavelength varies only weakly with particle size. Even when halving the optical thickness, the albedo is only slightly decreased (dotted black line). This is different for 1620 nm wavelength, where the albedo is not saturated (maximum about 0.28). In this case, halving the optical thickness has almost no effect (not shown). In contrast, halving the effective radius results in a largely increased albedo which differs from the measurements by 40–50%. From a radiative point of view, this does not confirm findings by *Garrett et al.* [2003], who suggested that the effective radius might be much smaller than usually assumed in climate models. For 1620 nm wavelength, the difference between the different representations of the scattering phase function in the radiative transfer model becomes much more obvious. While the differences between the exact phase function and the Henyey-Greenstein representation are seen, the Mie approximation deviates substantially, showing that the crystal shape has a nonnegligible impact at this wavelength.

[35] Table 1 shows the domain-averaged properties for the overcast cloud case. Optical thickness and effective radius were averaged over the nonempty pixels of the original MAS retrieval. The cloud cover relates to the ratio of nonempty pixels to total pixels in the model domain. The mean albedo was obtained by averaging the measurements or model results along the flight track from 20 to 250 km (overcast part).

[36] Figure 3 shows the domain-averaged measured and modeled spectrum of the cirrus albedo, using the Henyey-Greenstein approximation for the phase function 2. Again, only data from within 20–250 km were averaged for this plot. The solid line shows the SSFR measurements; the dotted lines indicate the variability of the albedo from 20 to 250 km (standard deviation). The symbols show the model calculations; the error bars show the modeled variability (standard deviation) within 20–250 km. For 745 nm and 1215 nm, the model results are slightly higher than measured. Otherwise, both mean value and standard deviation of measured and modeled albedo are in close agreement.

4.2. Broken Cloud Case

[37] The broken cloud case occurred on 23 July 2002 from 2259 to 2319 UTC. This case is more complex than the overcast case because (1) the surface has a considerable influence on the upwelling irradiance above cloud due to the low cloud optical thickness, and (2) several layers and multiple phases (water and ice) were detected. Figure 4 shows a false color image of the cloud scene, the MAS retrieved optical thickness, the vertical cloud structure as seen by the radar/lidar system, and the SSFR albedo. In the

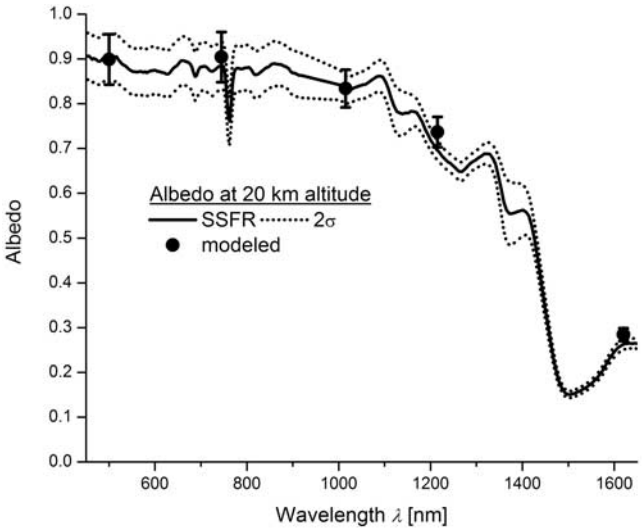

Figure 3. Measured and modeled domain average above the cloud covered part of the 9 July scene.

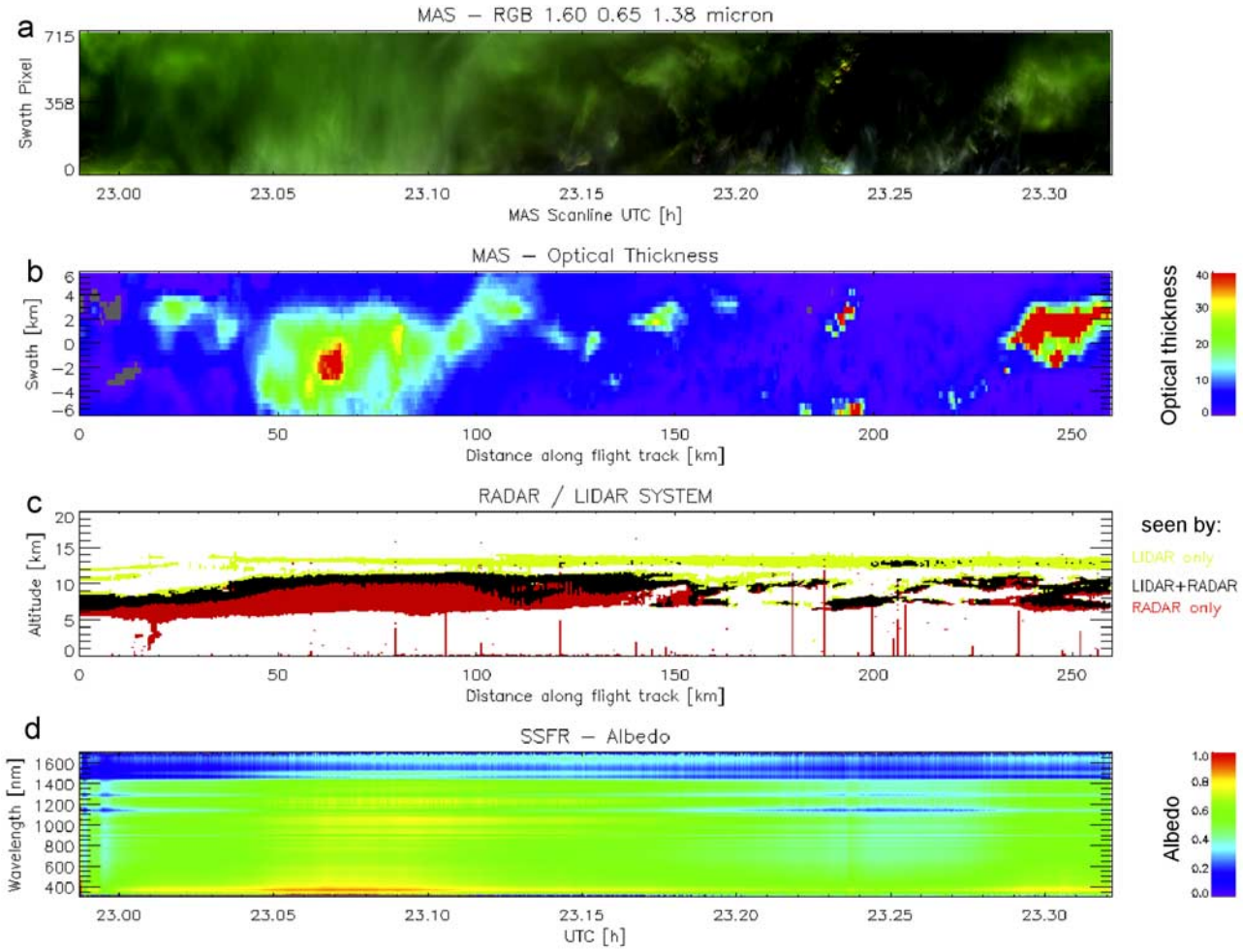

Figure 4. (a) MAS false color image, (b) retrieved cloud optical thickness, (c) vertical cloud extent as seen from lidar and radar, and (d) SSFR albedo along a leg of 270 km (2259–2319 UTC) on 23 July 2002, above a broken thin multilayer cirrus cloud. MAS optical thickness is shown for 500 m horizontal cloud resolution (τ_{max} = 150).

false color image in Figure 4a, the surface can be seen in some places. The cloud optical thickness ranged from 0.1 to 150 with an average of 8.1. Approximately 98% of the grid was covered by an optical thickness greater than 0.1 (see Table 2). In Figure 4c, the upper (green) layer is very thin, with small crystals, which are only detected by the lidar. The black layer is detected by both radar and lidar. Since the lidar can only penetrate layers of limited optical thickness, the lower (red) layer is only detected by the radar. The algorithm for obtaining the composite is described by *McGill et al.* [2004].

[38] Most of the leg occurred over land, with the remainder over sea, and a small segment over a lake. A two-dimensional surface albedo was assigned using the surface flag from MAS and SSFR surface albedo measurements above land and sea. For the lake, the sea surface albedo was used. In this case, neither periodic nor reflecting boundary conditions would be realistic, and a cloud-free scene beyond flight track might be more appropriate. This was simulated by an extended scene calculation where the MAS defined cloud grid was extended by off-swath zero optical thickness grid points.

[39] Figure 5 shows the SSFR measurements and modeling results for 500 nm (Figure 5, left) and 1620 nm (Figure 5, right). In addition, the MAS retrieved optical thickness, averaged over a footprint of 6 km radius (dash-dotted line), and the surface albedo, averaged over the same footprint, as well as the model results under cloud free

Table 2. Domain-Averaged Properties of the Broken Cloud Case

Property	Value
Cloud cover	98%
Optical thickness (nonempty points)	8.1
Effective radius (nonempty points)	43 μm
Cloud albedo	500 nm, 1620 nm
Measurement (SSFR, 20–250 km)	0.54, 0.30
Model results (20–250 km)	
With exact phase function	0.59, 0.34
With Henyey-Greenstein phase function	0.63, 0.38
With HG/single layer, single phase	0.63, 0.38
With spherical particles (Mie)	0.60, 0.36

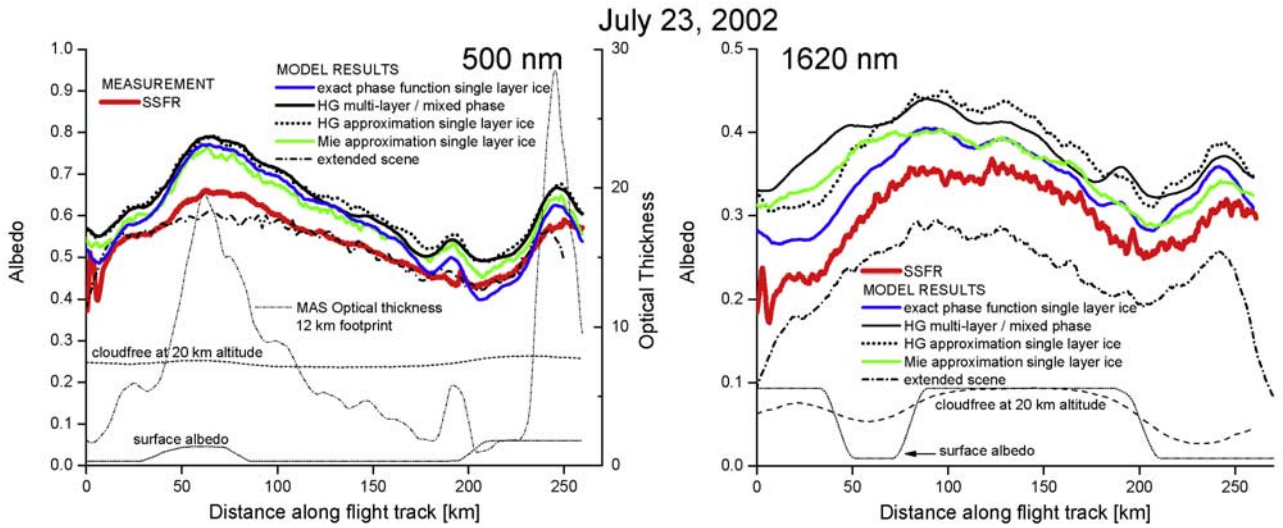

Figure 5. Measured and modeled albedo for 23 July 2002 for 500 nm and 1620 nm.

conditions are plotted for both wavelengths. The clear-sky albedo at 20 km altitude is much larger than the surface albedo because of Rayleigh scattering; for 1620, differences are due to geometrical smoothing. The model runs were performed using (1) the exact scattering phase function (blue line), (2) the Henyey-Greenstein approximation (black line), and (3) the Mie approximation (green line). For run types 1 and 3, a single-layer ice cloud was used; for run type 2, both the single-layer ice cloud and a two-layer mixed-phase cloud were used to examine the impact of multiple layers and/or mixed phase. For the two-layer mixed-phase cloud, a liquid water cloud was placed below the cirrus cloud layer for pixels where the MAS multilayer flag was raised. For grid points where the phase flag of MAS indicated liquid, the asymmetry parameter was calculated for spherical droplets using Mie theory.

[40] For 500 nm, there is, once again, almost no difference between irradiances calculated from the different representations of the scattering phase function. The measurements are always below the model results, except for a small area at around 210 km where the exact phase function results (blue line) fall below the measurements. One reason for this discrepancy may be that the MAS swath does not cover the entire SSFR footprint, but only about 71%. The other 29% percent of the measured irradiance emanates from areas beyond the MAS track. For this case, contrary to the overcast cloud case described in Section 4.1., the cloud description beyond the area observed by MAS may have differed considerably from the observed area. If no clouds had been present beyond the MAS swath then the modeled albedo (thick dash-dotted line, derived from run type 2: Henyey-Greenstein approximation, extended by off-swath pixels) would be in much closer agreement with the measurements. From 50 km to 100 km, the results from the extended scene with clear sky conditions beyond the MAS swath are below the measurements. This implies that an assumption of cloud-free regions beyond the MAS swath was too extreme, and suggests that some clouds were present.

[41] The same general picture is obtained for the long wavelength shown in Figure 5 (right). All model results are significantly larger than the measurements, except for the extended scene calculation, which is considerably lower than the measurements, showing again that the assumption of a cloud-free area beyond the MAS track is too extreme. The different representations of the scattering phase function are further apart. The disagreement between the single layer ice cloud (1, dotted black line) and the multilayer mixed-phase cloud (2, solid black line) is most pronounced before 60 km and between 100 km and 180 km. Before 60 km, a second liquid water cloud layer is present under the cirrus layer. Between 100 km and 180 km, up to 50% of the MAS swath is flagged as liquid. In this case, the exact phase function results are in close agreement with the measurements whereas the Henyey-Greenstein approximation overestimates the albedo with respect to the exact version. Interestingly, the results from the Mie representation and from the exact phase function almost coincide from about 80 km to 180 km. In this area, where big parts of the cloud are composed of spherical liquid water drops, the Mie phase function is obviously more appropriate than the Henyey-Greenstein approximation.

[42] Table 2 shows the domain averaged quantities of the broken cloud case. The high value for cloud cover is somewhat misleading because large areas of the model domain consist of an optical thickness below 1. Considering only boxes with optical thickness above 1 would result in a much lower cloud cover (71%).

5. Conclusions

[43] For two cases from CRYSTAL-FACE, we reconstructed cloud fields from MAS retrievals of two-dimensional fields of cirrus optical thickness and ice crystal effective radius. We then used the cloud fields in 3-D radiative transfer calculations and compared the simulated albedo along the flight track with SSFR measurements. We found that the calculated cloud albedo was in good agreement with SSFR measurements for the overcast cloud case with high

optical thickness. For the broken cloud case with low-moderate optical thickness, the measured cloud albedo was systematically below the model results. In some parts of the flight track, the discrepancy between measurement and simulation was up to 30%. This may be caused by contributions to irradiance that are beyond MAS swath and SSFR footprint. By applying periodic boundary conditions, we inherently assumed that outside of the MAS swath, cloud parameters are about the same as within. Using an extended scene with no clouds outside of the MAS swath demonstrated that the modeled cloud albedo can be lowered considerably, in closer agreement with the measurement. However, the 1620 nm calculations show that a completely cloud-free area beyond the MAS track is too extreme of an assumption.

[44] The different representations of the scattering phase function of the ice crystals have little or almost no impact on the visible wavelength simulation (500 nm). Likewise, the difference between the model results for mixed-phase versus ice phase and single-layer versus double-layer clouds is negligible for this wavelength. However, there is about 30% spread in the albedo simulations for the infrared wavelength (1620 nm). Moreover, a largely reduced effective radius throughout the cloud would increase the differences between measured and modeled cloud albedo at 1620 nm. Consequently, from a radiative perspective, we cannot confirm findings by *Garrett et al.* [2003].

[45] Overall, the 3-D structure of the two cloud cases had less impact on the model measurement agreement than expected; switching off horizontal photon transport had no effect on domain-averaged albedo, and independent pixel calculations would have sufficed to obtain budget-relevant parameters. The major differences between model and measurement are caused by (1) contributions from beyond the MAS swath and (2) the representation of the phase function in the radiative transfer model and hence by crystal shape. The discrepancies between SSFR measurements and model results are most pronounced for the broken cloud case and for the infrared wavelength (1620 nm).

[46] More systematic conclusions for a variety of cloud and surface conditions as well as solar zenith angles can only be drawn if the concept described in this study is applied to additional cases with concurrent spectral irradiance and spectral radiance imaging observations, for example, from experiments such as CRYSTAL-FACE and from a current field experiment in Costa Rica (TC4). MAS observations should be embedded in concurrent MODIS images to rule out the impact of off-swath contributions to spectral irradiance which turned out to be of substantial importance for the model results.

[47] **Acknowledgments.** The CRYSTAL-FACE experiment and this work were funded by the NASA Earth Science Enterprise Radiation Science Program. We are also grateful to Warren Gore, Larry Pezzolo, and Antony Trias from NASA Ames for their engineering and technical support of the SSFR instrument. Bernhard Mayer (German Space Agency, DLR) and Ronald Scheirer (Swedish Weather Service, SMHI) provided guidance on the usage of the radiative transfer models MYSTIC and GRIMALDI.

References

Ackerman, S. A., K. I. Strabala, W. P. Menzel, R. A. Frey, C. C. Moeller, and L. E. Gumley (1998), Discriminating clear sky from clouds with MODIS, *J. Geophys. Res.*, *103*, 32,141–32,158.

Anderson, G. P., J. H. Chetwynd, S. A. Clough, E. P. Shettle, and F. X. Kneizys (1986), AFGL atmospheric constituent profiles (0–120 km), *Tech. Rep. AFGL-TR-86-0110*, Accession ADA175173, Air Force Geophys. Lab., Hanscom AFB, Mass.

Ardanuy, P. E., L. L. Stowe, A. Gruber, and M. Weiss (1991), Shortwave, longwave, and net cloud-radiative forcing as determined from Nimbus 7 observations, *J. Geophys. Res.*, *96*, 18,537–18,549.

Barkstrom, B. R. (1984), The Earth Radiation Budget Experiment (ERBE), *Bull. Am. Meteorol. Soc.*, *65*, 1170–1185.

Baum, B. A., P. Yang, A. J. Heymsfield, S. Platnick, M. D. King, Y.-X. Hu, and S. T. Bedka (2005), Bulk scattering properties for the remote sensing of ice clouds II: Narrowband models, *J. Appl. Meteorol.*, *44*, 1896–1911.

Derber, J. C., D. F. Parrish, and S. J. Lord (1991), The new global operational analysis system at the National Meteorological Center, *Weather Forecast.*, *6*, 538–547.

Garrett, T. J., H. Gerber, D. G. Baumgardner, C. H. Twohy, and E. M. Weinstock (2003), Small, highly reflective ice crystals in low-latitude cirrus, *Geophys. Res. Lett.*, *30*(21), 2132, doi:10.1029/2003GL018153.

Hock, T. F., and J. L. Franklin (1999), The NCAR GPS dropwindsonde, *Bull. Am. Meteorol. Soc.*, *80*, 407–420.

Kiehl, J. T., J. J. Hack, and B. P. Briegleb (1994), The simulated Earth radiation budge of the National Center for Atmospheric Research community climate model CCM2 and comparisons with the Earth Radiation Budget Experiment (ERBE), *J. Geophys. Res.*, *99*, 20,815–20,828.

King, M. D., Y. J. Kaufman, W. P. Menzel, and D. Tanre (1992), Remote-sensing of cloud, aerosol, and water-vapor properties from the Moderate Resolution Imaging Spectrometer (MODIS), *IEEE Trans. Geosci. Remote Sens.*, *30*, 2–27.

King, M. D., S. Platnick, P. Yang, G. T. Arnold, M. A. Gray, J. C. Riedi, S. A. Ackerman, and K. N. Liou (2004), Remote sensing of liquid water and ice cloud optical thickness and effective radius in the arctic: Application of airborne multispectral MAS data, *J. Atmos. Oceanic Technol.*, *21*, 857–875.

Kurucz, R. L. (1992), Synthetic infrared spectra, in *Infrared Solar Physics: Proceedings of the International Astronomical Union*, *IAU Symp.*, vol. 154, edited by D. M. Rabin, J. T. Jefferies, and C. Lindsey, pp. 523, Kluwer Acad., Norwell, Mass.

Loeb, N. G., S. Kato, K. Loukachine, and N. Manalo-Smith (2005), Angular distribution models for top-of-atmosphere radiative flux estimation from the clouds and the Earth's radiant energy system instrument on the Terra satellite. part I: Methodology, *J. Atmos. Oceanic Technol.*, *22*, 338–351.

Mayer, B. (1999), I3RC phase 1 results from the MYSTIC Monte Carlo model, paper presented at I3RC Workshop, Clim. Radiat. Branch, NASA Goddard Lab. Atmos., Tucson, Ariz.

Mayer, B., and A. Kylling (2005), The libRadtran software package for radiative transfer calculations—Description and examples of use, *Atmos. Chem. Phys.*, *5*, 1855–1877.

McGill, M. J., L. Li, W. D. Hart, G. M. Heymsfield, D. L. Hlavka, P. E. Racette, L. Tian, M. A. Vaughan, and D. M. Winker (2004), Combined lidar-radar remote sensing: Initial results from CRYSTAL-FACE, *J. Geophys. Res.*, *109*, D07203, doi:10.1029/2003JD004030.

Menzel, W. P., W. L. Smith, and T. R. Stewart (1983), Improved cloud motion wind vector and altitude assignment using VAS, *J. Appl. Meteorol.*, *22*, 377–384.

Pilewskie, P., and S. Twomey (1987), Cloud phase discrimination by reflectance measurements near 1.6 and 2.2 μm, *J. Atmos. Sci.*, *44*, 3419–3420.

Pilewskie, P., J. Pommier, R. Bergstrom, W. Gore, S. Howard, M. Rabbette, B. Schmid, P. V. Hobbs, and S. C. Tsay (2003), Solar spectral radiative forcing during the Southern African Regional Science Initiative, *J. Geophys. Res.*, *108*(D13), 8486, doi:10.1029/2002JD002411.

Platnick, S. (2000), Vertical photon transport in cloud remote sensing problems, *J. Geophys. Res.*, *105*, 22,919–22,935.

Platnick, S., J. Y. Li, M. D. King, H. Gerber, and P. V. Hobbs (2001), A solar reflectance method for retrieving the optical thickness and droplet size of liquid water clouds over snow and ice surfaces, *J. Geophys. Res.*, *106*, 15,185–15,200.

Platnick, S., M. D. King, S. A. Ackerman, W. P. Menzel, B. A. Baum, J. C. Riedi, and R. A. Frey (2003), The MODIS cloud products: Algorithms and examples from Terra, *IEEE Trans. Geosci. Remote Sens.*, *41*, 459–473.

Ramanathan, V., R. D. Cess, E. F. Harrison, P. Minnis, B. R. Barkstrom, E. Ahmad, and D. Hartmann (1989), Cloud-radiative forcing and climate—Results from the Earth Radiation Budget Experiment, *Science*, *243*, 57–63.

Scheirer, R., and A. Macke (2001), On the accuracy of the independent column approximation in calculating the downward fluxes in the UVA, UVB, and PAR spectral ranges, *J. Geophys. Res.*, *106*, 14,301–14,312.

Schmidt, S., V. Venema, F. Di Giuseppe, R. Scheirer, M. Wendisch, and P. Pilewskie (2007), Reproducing cloud microphysical and irradiance measurements using three 3D cloud generators, *Q. J. R. Meteorol. Soc.*, *133*, 765–780.

Soden, B. J., and I. M. Held (2006), An assessment of climate feedbacks in coupled ocean-atmosphere models, *J. Clim.*, *19*, 3354–3360.

Takano, Y., and K. N. Liou (1989), Solar radiative transfer in cirrus clouds. 1. Single-scattering and optical properties of hexagonal ice crystals, *J. Atmos. Sci.*, *46*, 3–19.

Twomey, S., and T. Cocks (1982), Spectral reflectance of clouds in the near-infrared: Comparison of measurements and calculations, *J. Meteorol. Soc. Jpn.*, *60*, 583–592.

van de Hulst, H. C. (1980), *Multiple Light Scattering: Tables, Formulas, and Applications*, Academic, New York.

Wendisch, M., P. Pilewskie, E. Jäkel, S. Schmidt, J. Pommier, S. Howard, H. H. Jonsson, H. Guan, M. Schröder, and B. Mayer (2004), Airborne measurements of areal spectral surface albedo over different sea and land surfaces, *J. Geophys. Res.*, *109*, D08203, doi:10.1029/2003JD004392.

Wendisch, M., P. Pilewskie, J. Pommier, S. Howard, P. Yang, A. J. Heymsfield, C. G. Schmitt, D. Baumgardner, and B. Mayer (2005), Impact of cirrus crystal shape on solar spectral irradiance: A case study for subtropical cirrus, *J. Geophys. Res.*, *110*, D03202, doi:10.1029/2004JD005294.

Wielicki, B. A., et al. (1998), Clouds and the Earth's Radiant Energy System (CERES): Algorithm overview, *IEEE Trans. Geosci. Remote Sens.*, *36*, 1127–1141.

Yang, P., and K. N. Liou (1996), Geometric optics integral equation method for light scattering by nonspherical ice crystals, *Appl. Opt.*, *35*, 6568–6584.

P. Pilewskie and K. S. Schmidt, Laboratory for Atmospheric and Space Physics, University of Colorado, Boulder, CO 80309-0311, USA. (sebastian.schmidt@lasp.colorado.edu)

S. Platnick and G. Wind, NASA Goddard Space Flight Center, Code 913, 8800 Greenbelt Road, Greenbelt, MD 20771, USA.

M. Wendisch, Institute for Atmospheric Physics, Johannes Gutenberg University of Mainz, Becherweg 21, Mainz D-55099, Germany.

P. Yang, Department of Atmospheric Sciences, Texas A&M University, 3150 TAMU, College Station, TX 77843, USA.